

Factors determining electrostatic fields in molecular dynamics simulations of the Ras/effector interface

Daniel L. Ensign and Lauren J. Webb*

Department of Chemistry and Biochemistry, Center for Nano- and Molecular Science and Technology, and Institute for Cell and Molecular Biology, The University of Texas at Austin, Austin, Texas 78712

ABSTRACT

Using molecular dynamics simulations, we explore geometric and physical factors contributing to calculated electrostatic fields at the binding surface of the GTPase Ras with a spectroscopically labeled variant of a downstream effector, the Ras-binding domain of Ral guanine nucleotide dissociation stimulator (RalGDS). A related system (differing by mutation of one amino acid) has been studied in our group using vibrational Stark effect spectroscopy, a technique sensitive to electrostatic fields. Electrostatic fields were computed using the AMBER 2003 force field and averaged over snapshots from molecular dynamics simulation. We investigate geometric factors by exploring how the orientation of the spectroscopic probe changes on Ras-effector binding. In addition, we explore the physical origin of electrostatic fields at our spectroscopic probe by comparing contributions to the field from discrete components of the system, such as explicit solvent, residues on the Ras surface, and residues on the RalGDS surface. These models support our experimental hypothesis that vibrational Stark shifts are caused by Ras binding to its effector and not the structural rearrangements of the effector surface or probe reorientation on Ras-effector binding, for at least some of our experimental probes. These calculations provide physical insight into the origin, magnitude, and importance of electrostatic fields in protein–protein interactions and suggest new experiments to probe the field's role in protein docking.

Proteins 2011; 79:3511–3524.
© 2011 Wiley-Liss, Inc.

Key words: p21Ras; vibrational stark effect spectroscopy; molecular dynamics simulation; electrostatics calculations.

INTRODUCTION

The protein p21^{Ras} (hereafter Ras) hydrolyzes guanosine triphosphate (GTP) as part of several fundamental regulatory cycles, which impact cell proliferation, cell survival, and apoptosis.^{1–4} Mutations to Ras that effect its signaling function are associated with 30% of human cancer tumors, and for this reason, Ras has been a central focus of molecular oncology research for decades.^{3,5–8} When bound to GTP, Ras binds to various downstream effectors in the propagation of several different signaling pathways; one such effector is the Ras-binding domain of Ral guanine nucleotide dissociation stimulator (RalGDS, hereafter Ral). These two proteins dock without the formation of a covalent bond, meaning the factors that influence the free energy and kinetics of the interaction are entirely due to structural complementarity and electrostatic fields generated by these proteins' charge distributions. We have previously demonstrated the experimental utility of this system as a probe of the role and mechanism of electrostatic fields on interface formation.⁹

Our experimental studies used vibrational Stark effect (VSE) spectroscopy^{10–16} to investigate Ras-Ral binding.⁹ VSE spectroscopy relates the change in vibrational frequency $\Delta\nu$ of a harmonic oscillator to changes in the electrostatic field $\Delta\vec{F}$ upon perturbation, such as a protein docking to a downstream effector, through a proportionality constant $\Delta\vec{\mu}$, called the Stark tuning rate:

$$\Delta\nu = -\Delta\vec{\mu} \cdot \Delta\vec{F} \quad (1)$$

This relationship reduces to $\Delta\nu = -\Delta\mu\Delta F$ for a linear probe such as the nitrile oscillator, for which the Stark tuning rate (the difference dipole moment) points from the nitrogen atom to the carbon atom (Fig. 1). ΔF is the change in the component of the electric field parallel to the bond. The vibrational Stark effect relates a readily measured quantity (the change in vibrational energy upon perturbation) with a

Additional Supporting Information may be found in the online version of this article.

The authors state no conflict of interest.

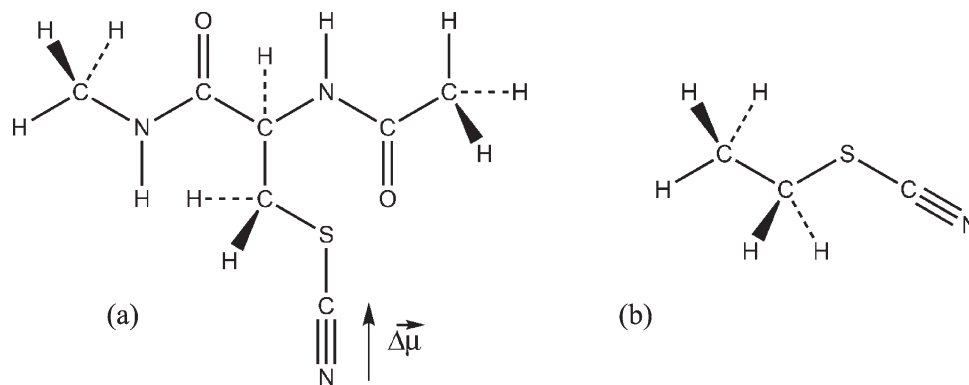
Grant sponsor: Burroughs Wellcome Fund; Grant number: 1007207.01; Grant sponsor: The Welch Foundation; Grant number: F-1722.

*Correspondence to: Lauren J. Webb, Department of Chemistry and Biochemistry, Center for Nano- and Molecular Science and Technology, and Institute for Cell and Molecular Biology, The University of Texas at Austin, 1 University Station A5300, Austin, Texas 78712. E-mail: lwebb@cm.utexas.edu.

Received 7 January 2011; Revised 18 April 2011; Accepted 4 May 2011

Published online 20 May 2011 in Wiley Online Library (wileyonlinelibrary.com).

DOI: 10.1002/prot.23095

**Figure 1**

(a) Methyl-capped cyanocysteine residue used for RESP charge fitting. The nitrile difference dipole (Stark tuning rate) $\Delta\vec{\mu}$ is illustrated. (b) Ethylthiocyanate is used for validating the AMBER ff03 force field for the cyanocysteine residue.

theoretical quantity $\Delta\vec{F}$ that can be calculated by a variety of methods, such as the protein dipoles-Langevin dipoles method,¹⁷ solutions to the Poisson–Boltzmann equation,^{18–21} and the Coulomb interactions defined by a molecular mechanics force field.^{22–26}

In previous work, we used VSE spectroscopy to draw an experimental map of electrostatic fields at the interface of Ras docked with the downstream effector Ral.⁹ In these experiments, the nitrile VSE probe was introduced through systematic mutation of 11 residues at the surface of Ral to cysteine; these residues (illustrated in Fig. 2) were chosen because of their location within the interfacial region formed when Ras docks to Ral. These cysteines were chemically modified to cyanocysteine, and the vibrational frequency of the nitrile was measured for each labeled Ral mutant first in the monomeric form, and then after incubation with Ras to form the docked complex. Measurements of this kind provide a unique experimental benchmark of calculations of electric field, and complement ¹⁹F nuclear resonances or pK_a titrations^{27–35} which previously have been used to estimate local electrostatic environments in the protein interior, but which are often a convolution of electrostatic and covalent influences.

If the calculations yield electric fields consistent with experiment, they have the potential to illuminate details of the electrostatic field that cannot be addressed experimentally, such as determining which parts of the system (protein, solvent, etc.) contribute most to the field at any location. Additionally, the results of such calculations can provide a means for interpretation of existing experimental data and for designing new experiments. In this article, we explore each of these ideas by simulation of the docking of Ral and a variant of Ras, Ras E31K, and test the geometric and physical contributions to electrostatic fields at the Ras–Ral interface. Using molecular dynamics (MD) simulations, we consider geometric factors and

their influence on field by exploring how the orientation of the spectroscopic probe changes on complexation of Ras to its downstream effector. We calculate electric fields experienced by the probe in order to explore contributions to these fields from Ral amino acid residues, Ras amino acid residues, and explicit solvent. Taken together, these calculations suggest that although structural rearrangements occur on binding, the largest contributors to changes in electrostatic fields at the spectroscopic probe are due to the removal of solvent and formation of the Ras–Ral interface.

Preliminary work underway in our laboratory has suggested that the fields we calculate here correlate well to electrostatic fields measured using the vibrational Stark effect on the Ras–Ral system. A detailed comparison will be reported in a further publication. Because of these correlations, predictions from the present calculations are suitable to guide future experiments on this system. Broadly, these calculations allow us to explore the physical mechanism for the origin of the Stark effect at the Ras–Ral interface in atomic detail. In this work, we examine the different contributions to the electrostatic field at the Ras–effector interface, not merely the whole field, and discuss vibrational Stark effect experiments that test directly the detailed predictions of electrostatics calculations.

METHODS

Modeling of the cyanocysteine residue and GDPNP

Cyanocysteine partial charges were derived using the restrained electrostatic potential (RESP) method,^{36,37} as previously described.⁹ Briefly, GAMESS^{38,39} was used to run restricted Hartree–Fock calculations with the 6-31g* basis set (RHF/6-31g*) on 12 side chain rotamers of the

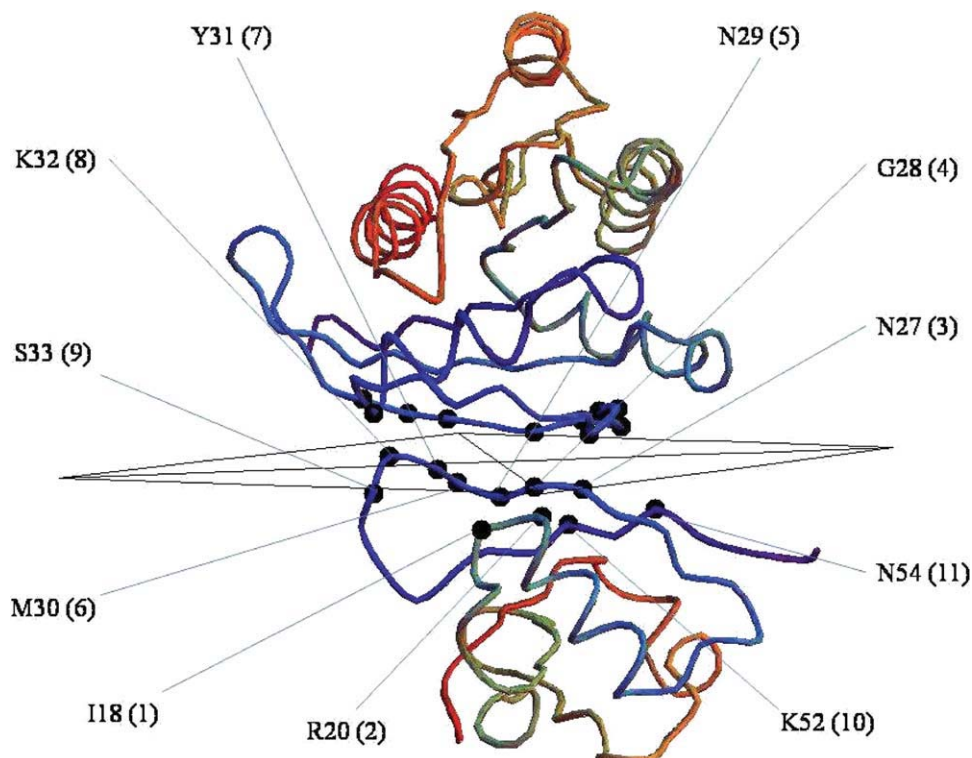


Figure 2

The binding surface used for geometric calculations in this work, relative to the Ras-Ral structure in pdb 1LFD. Ral residues, which are labeled in our experiments, are indicated, along with index numbers corresponding to labels in Figures 6–8. The Ras and Ral C α atoms used to compute the surface plane are shown as spheres.

capped cyanocysteine fragment shown in Figure 1. The resulting electrostatic potentials were used for two-stage RESP fitting. Other cyanocysteine parameters were transferred directly from the Amber 2003 force field²⁴ files to the ffamber03 GROMACS⁴⁰ port.⁴¹ The charges and atom types are summarized elsewhere.⁹

To test the accuracy of our cyanocysteine charge model, we computed the Hartree–Fock (RHF/6-31g*) energy as a function of torsion around the sulfur-carbon bond of ethylthiocyanate, with the alkane hydrogens ideally staggered, as illustrated in Figure 1. This was compared with the AMBER ff03 energy for the same molecule, using the charges we derived using RESP for the cyanocysteine side chain; the total backbone charge of cyanocysteine was divided equally among the methyl hydrogens. The comparison is shown in Supporting Information Figure S1. With the trans conformation as the zero of energy, the energy near the gauche conformations of -60° and 60° were 1.79 kJ/mol higher in the quantum mechanical (QM) calculation than in AMBER; compared with the -180° trans conformation, these minima were ~ 3.28 kJ/mol in QM and 1.65 kJ/mol in AMBER. The Boltzmann factor at 300 K is 0.25 for the gauche conformations in QM compared with 0.5 in AMBER. Therefore, gauche conformations are over-represented in simu-

lations using the AMBER force field, but the overall agreement of the two energy calculations is reasonable.

In our experiments, the Ras molecule contains the nonhydrolyzable GTP analog guanosine 5'-[β , γ -imido]-triphosphate (GDPNP). Atom types for GDPNP were taken to be the same as the ffamber03 atom types for GTP, except for the phosphate-bridging nitrogen atom (N3B), which was assigned Amber atom-type N2 (GROMACS ffamber03 atom type ffamber99_38) by Antechamber.^{42,43} This atom type is described as “sp² N in amino groups” in the Amber file parm99.dat; it is the only sp²-hybridized nitrogen atom type in AMBER, which is not intended for amide groups or rings.

We used a two-stage method for obtaining GDPNP charges: MD simulation with an initial guess of charges, followed by multiconformer RESP fitting of the structures obtained from simulation. For the first stage, preliminary GDPNP charges were generated by running RHF/4-31g calculations with GAMESS, using the GDPNP coordinates from pdb file 1LFD with hydrogen added using the GROMACS utility pdb2gmx. Two-stage RESP fitting was then used to generate preliminary charges. This charge model was used to generate a 10-ps molecular dynamics simulation of Ras (from 1LFD) containing GDPNP and Mg²⁺ in a continuum solvent with

$\varepsilon = 78$, using the stochastic dynamics integrator with 2-fs time steps at 300 K with an inverse friction coefficient of 1, explicit calculation of all Coulomb and van der Waals interactions, and constraining bonds to hydrogen with SHAKE. Eleven GDPNP conformations (including the $t = 0$ ps structure) collected at 1-ps intervals were input to GAMESS to run RHF/4-31g calculations using Pulay's DIIS interpolation.⁴⁴ The electronic wave functions obtained were used as initial guesses for RHF/6-31g* calculations required for multiconformer, two-stage RESP fitting. The charges thus obtained and a summary of the ffamber03 atom types for GDPNP are shown in Supporting Information Table S1.

Construction and simulation of protein systems

Labeled Ral β mutants

In this work, we refer to simulations of Ral mutants described in full detail elsewhere.⁹ Briefly, the Ral molecule from pdb 2RGF was used as a starting point, whereupon (1) the two cysteines were changed to alanine by deletion of cysteine heavy atoms, (2) ALA and LEU beginning the 2RGF structure were changed to SER and HIS by renaming the residues and atoms and modeling in the heavy atoms using the AMBER utility *tleap*,⁴⁵ (3) an N-terminal glycine was added using *Avogadro*,⁴⁶ and (4) C-terminal residues RTFT were taken from 1RAX, after aligning the sequence KKRT, which terminates 2RGF to the same residues in 1RAX. Cyanocysteine mutations were generated by modeling residues as methionine (which contains the same number of heavy atoms as cyanocysteine) using *tleap*. The hydrogens were then deleted, and the residue and atom names were changed to be consistent with cyanocysteine. A gentle energy minimization was used to straighten the thiocyanate group. The locations of these SCN-labeled residues on the Ral surface are shown in Figure 2.

After energy minimization of these Ral mutant models in vacuum, solvation with *tip3p* water,⁴⁷ addition of neutralizing sodium ions, and equilibration, as described previously, eight rotamers about the cyanocysteine C β –S γ bond were generated for each mutant at torsions of -180° , -135° , -90° , -45° , 0° , 45° , 90° , and 135° . For sampling, these torsions were maintained with dihedral restraint potentials centered at each value, flat within 45° of the center, and quadratic with a force constant of $1,000 \text{ kJmol}^{-1} \text{ radian}^{-2}$ outside of that range. Eight 1-ns trajectories with those restraint potentials and one unrestrained trajectory were generated using the stochastic dynamics integrator in GROMACS. Using the weighted histogram analysis method (WHAM),^{48,49} the probe torsional distribution was found to have an alkane-like structure with maxima near -180° , -60° , and 60° and minima near -120° , 0° , and 120° . For each mutant, three additional simulations were started from

snapshots near each of the three free energy minima to generate the trajectories we call the “second stage” monomer simulations. These additional simulations were 3 ns in length, yielding a total of 18 ns of simulation for each SCN-labeled Ral mutant. Snapshots collected at 5-ps intervals from each simulation (3,600 snapshots per mutant) were used for Poisson–Boltzmann and explicit solvent calculations of electric field.

Construction of the Ras molecule

The N-terminal residues (sequence GAMGS) on Ras were modeled starting with pdb structure 1LFD, for which the sequence begins with MTEY. A search of the Protein Data Bank identified 87 pdb files which began with GAMGS, consisting of 192 structures. Of these structures, 102 had coordinates for (at least) all heavy atoms of GAMGS. The coordinates for the N, C α , C, and O atoms of the residues after GAMGS in these 102 sequences were aligned to the four backbone atoms of the N-terminal methionine of the 1LFD Ras structure in VMD.⁵⁰ These aligned N-termini were added to Ras from 1LFD, the energy of each modified Ras was calculated in the ffamber03 force field after adding hydrogen atoms using the GROMACS utility *pdb2gmx*, and the lowest energy conformation was chosen as the model of the N-terminal residues of Ras.

Simulations Ras-labeled Ral-docked complex

The docked complex was generated by alignment of the structures from the 3-ns second-stage simulations of monomeric labeled Ral mutants. The cyanocysteine torsional free energy surface, derived from these simulations using WHAM, was fitted by least-squares to a Fourier sine series truncated at the fourth term. The global minimum of these surfaces was found to be close to the trans conformation (-180°) for the labeled Ral mutants I18C_{SCN}, R20C_{SCN}, N27C_{SCN}, G28C_{SCN}, M30C_{SCN}, Y31C_{SCN}, K32C_{SCN}, S33C_{SCN}, and N54C_{SCN}. The minima were -65.9° for Ral N27C_{SCN} and -63.8° for Ral K52C_{SCN}. The structural snapshot from the second stage monomeric SCN-labeled Ral simulations with the cyanocysteine torsion closest to this minimum was aligned to the RalGDS model in 1LFD using STAMP structural alignment⁵¹ in VMD, with the exception of N54C_{SCN}.

Modeled N-terminal residues of the labeled Ral mutant structures overlapped in space with Ras helix 1 atoms. For 10 of the 11 labeled Ral mutant constructs, this overlap consisted of the modeled N-terminus of Ral being too close to the N-terminal end of helix 1 of Ras; for N54C_{SCN}, the N-terminal strand threaded into the Ras fold. For this reason, a new Ral N54C_{SCN} model was chosen by taking the N54C_{SCN} structure second closest to the cyanocysteine torsional free energy minimum. Like the other mutants, this model's Ral N-terminus was too

close to the Ras helix. To relax the clashes in these 11 models with the Ras helix, steepest descents minimization was used while constraining all atoms of Ras, Ral, and GDPNP including the Mg^{2+} ion to their starting positions, except for the 155 atoms constituting the first 10 residues of Ral, using a harmonic potential with a force constant of $1,000 \text{ kJ mol}^{-1} \text{ nm}^{-2}$ in the three Cartesian directions. This energy minimization consisted of 1,000 steps of steepest descents with an initial step size of 0.01 nm, explicitly calculating all van der Waals and Coulomb interactions.

The 11 constructs generated in this way were then energy minimized, solvated, and equilibrated exactly as described above for the Ral mutants, with the exception that restraint angles for the cyanocysteine side chain were used at -180° to 120° in steps of 60° in anticipation of the alkane-like structure of the free energy surface. Six 2-ns trajectories, with the cyanocysteine $\text{C}\beta\text{-S}\gamma$ torsion constrained at each angle, were generated for each labeled Ral mutant docked to Ras, totalling 12 ns per mutant. We will henceforth refer to these trajectories as the “docked complex” trajectories. Snapshots collected at 5-ps intervals from each simulation (2,400 snapshots per mutant) were used for Poisson–Boltzmann and explicit solvent calculations of electric fields.

Probe torsional distributions

The molecular dynamics simulations of the monomer and docked complex with cyanocysteine $\text{C}\beta\text{-S}\gamma$ torsions restrained were interpreted using WHAM. This resulted in torsional probability distributions at 300 K from these simulations in 72 bins of width 5° for the 11 docked complexes. Simulation degrees of freedom (e.g., electric fields) were averaged over these distributions. WHAM gave the probability p_i of the torsion occupying bin i , one of seventy-two 5° bins around the $\text{C}\beta\text{-S}\gamma$ dihedral angle (with the -180° bin containing -180° at its left endpoint). The average magnitude of the electric field component parallel to the probe $F = |\vec{F}|$ was calculated as

$$\langle F \rangle = \sum_{i=1}^{72} p_i \langle F \rangle_i \quad (2)$$

where $\langle F \rangle_i$ is the arithmetic mean of field components parallel to the bond at torsions contained in bin i , calculated as described below. As we only discuss the average electric field in this work, we will drop the brackets indicating averaging and write $F = \langle F \rangle$. Electric fields should be understood as electric field components at the nitrile and parallel to the nitrile bond.

Explicit solvent calculations of electric field

After generation of simulation snapshots of SCN-labeled Ral in the monomeric and docked complex states, the electric field due to the Coulomb portion of

the force field was calculated for each snapshot. A particle with charge +1 and zero van der Waals interactions was placed on the nitrile bond halfway between the carbon and nitrogen atoms. The force on this particle was calculated using the “-rerun” facility of the GROMACS molecular dynamics engine, *mdrun*. The component of the field parallel to the nitrile served as the computational representation of the experimental observable. These fields were averaged using the torsional probability distribution derived from WHAM.

The field calculation included scaled Coulomb forces on the test charge due to protein atoms and tip3p explicit water. A reaction field treatment was used for electrostatic interactions in a periodic system, using a short-range dielectric $\epsilon_r = 1$, a long-range dielectric $\epsilon_{rf} = 78$, and a scaling length $r_c = 1.0 \text{ nm}$.⁵² (Refer to ref. 52 and the Results section for the formulas representing the long-range electrostatics treatment.)

The nitrile charges were not included in the explicit solvent field calculations. The AMBER ff03 nitrile bond has a large force constant of $848,930.0 \text{ kJ mol}^{-1} \text{ nm}^{-2}$ (compared with, e.g., $392,459.2 \text{ kJ mol}^{-1} \text{ nm}^{-2}$ for C–C), which ensures that the nitrile bond length does not change significantly during the course of simulation, and therefore, the nitrile atoms have approximately constant contribution to the electric field at the nitrile midpoint. For this reason, the charges of the nitrile carbon and nitrogen atoms were set to zero. The magnitude of the field due to the AMBER charges is large, $1,381.95 \text{ kT/e}\text{\AA}$ (calculated assuming the reference length of 0.1138 nm and using Coulomb’s law). Ignoring the nitrile charges eliminated a large contribution to the electric field at the nitrile midpoint, increasing the numerical accuracy of the calculation of field differences.

RESULTS

Probe torsional probability distributions

Because electric fields are a vector quantity and the chemically modified cysteine residue contains two free torsions, the probe’s orientational probability distribution is needed to calculate the vibrational Stark effect in this system. The probability distribution of each probe’s $\text{C}\beta\text{-S}\gamma$ torsion, derived by applying WHAM to all trajectories of Ral mutants in the monomeric form and docked to Ras, are shown in Supporting Information Figure S2. The general structure of these distributions was unsurprisingly like an alkane, with peaks at the trans (-180°) and gauche (-60° and 60°) conformations, in both the monomer and the docked complex.

In most cases, the probability distribution for the docked complex was similar to the monomer, to the point of having similar fine structure. For example, both monomer and docked complex distributions for Ral

N29C_{SCN} had a split peak near the -60° orientation. In other cases, different fine structure appeared or disappeared on binding, as in Ral K52C_{SCN}, where one peak in the monomer probability density near the -60° orientation split into two peaks in the docked complex. In four labeled Ral mutants, R20C_{SCN}, Y31C_{SCN}, K32C_{SCN}, and S33C_{SCN}, the difference between distributions was more dramatic, as these mutants showed a large increase in the trans density on binding. These results highlight the complexity and variability of the protein environment, compared with what might be expected for an alkane in the fluid phase.

Errors of the probability of any torsional bin due to sampling were small, on the order of 10^{-6} , according to a Monte Carlo simulation of the WHAM posterior distribution of the bin free energies (data not shown). However, this estimate only takes into account the sampling in a bin at equilibrium. To assess the error due to violating the equilibrium assumption of WHAM, we calculated the probability distribution for each mutant using the first half of the 12 trajectories (first 9 ns) for each monomer, and the six trajectories (first 6 ns) of each docked complex, compared with distributions derived from the latter half of each trajectory. We found that the probability distributions change very little in the latter stages of our simulations (Supporting Fig. S3 and S4 show these distributions for the monomer and docked complex, respectively). In most bins, the probability changed by less than 0.01, although a minority of bins changed probability by 0.01–0.02. Although the errors in the probability could be larger if the monomer or the docked complex were exploring metastable regions of phase space, the persistence of structure in these distributions is consistent with local equilibration. Moreover, the general agreement of our electrostatics calculations with experiment, discussed below, suggests that such errors are not significant. The role of sampling in these calculations will be the subject of further work.

Orientation of the probe

To examine in detail, the probe orientation and how it changes on binding to Ras, we calculated the average (using the Boltzmann distributions from WHAM) “azimuthal” and “polar” angles of the nitrile probe in our molecular dynamics simulations. To compute the azimuthal angle θ (Fig. 3), a model binding surface was defined for the Ras-Ral docked complex in the following way. A Ral surface plane was constructed by least-squares fitting to the coordinates of C α atoms of the Ral surface residues I18, R20, N27, G28, N29, M30, Y31, K32, S33, K52, and N54 in pdb 1LFD. A similar plane was constructed for the Ras surface using residues Q25, D33, P34, T35, I36, E37, D38, Y40, R41, and K42. The binding surface was taken to be the average of the Ral plane with the Ras plane and is illustrated in the context of the Ras-

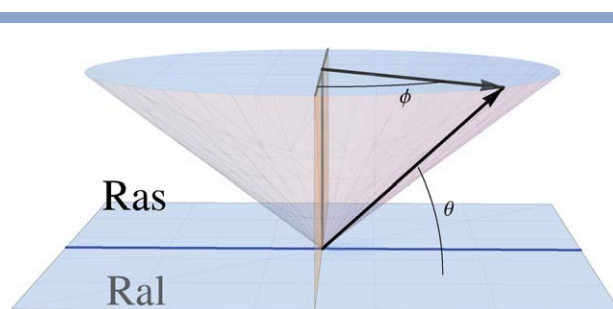


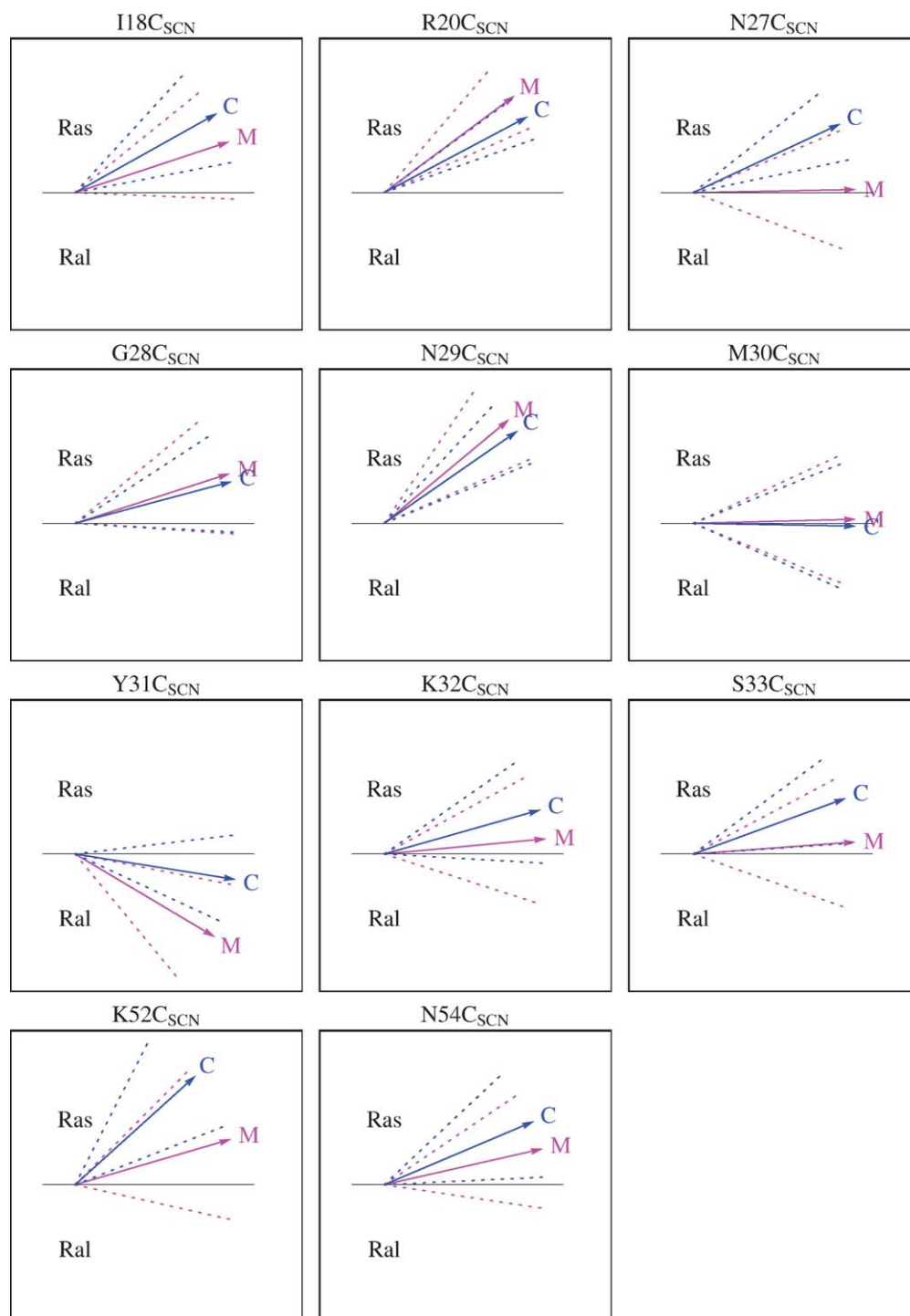
Figure 3

Cartoon of surfaces. The binding surface lies between the Ras and Ral molecules as it was defined by the average of a plane fit through Ras C α atoms and a plane fit through Ral C α atoms. The azimuthal angles θ , shown in Figure 4, are relative to this plane. The polar axis is shown in blue; polar angles ϕ shown in Figure 5 are relative to the vertical plane shown, which is perpendicular to the binding surface and the surface axis.

Ral pdb structure 1LFD in Figure 2. The binding surface is also illustrated schematically in Figure model of surfaces. The polar angle ϕ (Fig. 3) of the nitrile probe on the surface was defined relative to an axis on the binding surface. This surface axis was defined by the intersection of the binding surface with a vertical plane constructed by least-squares fitting to all α carbons of the pdb 1LFD. (Note that this vertical plane is not perpendicular to the binding surface.) The polar angle was first taken as the angle between the polar axis and the projection of the nitrile bond vector onto the binding surface. This angle was subsequently subtracted from 90° to obtain an angle from a plane perpendicular to both the binding surface and the surface axis.

The θ and ϕ angles were computed for each structural snapshot from MD aligning of the structure to the Ral structure in 1LFD, using STAMP structural alignment⁵¹ in VMD.⁵⁰ After alignment, a custom utility based on the GROMACS⁴⁰ template.c code was used to compute the dot product of a normal to this surface with the nitrile bond vector $\vec{r} = \vec{r}_N - \vec{r}_C$; that is, with the vector pointing from the carbon atom to the nitrogen atom of the nitrile. The angles were computed by taking the inverse cosine of the dot product; the inverse cosine of the dot product of any bond vector with a surface normal returns an angle in the range $(0^\circ, 180^\circ)$, so the angles a probe makes to each plane are reported in the range $(-90^\circ, 90^\circ)$. These angles were subsequently averaged for each Ral mutant using the Boltzmann distributions of the probe torsion derived from WHAM.

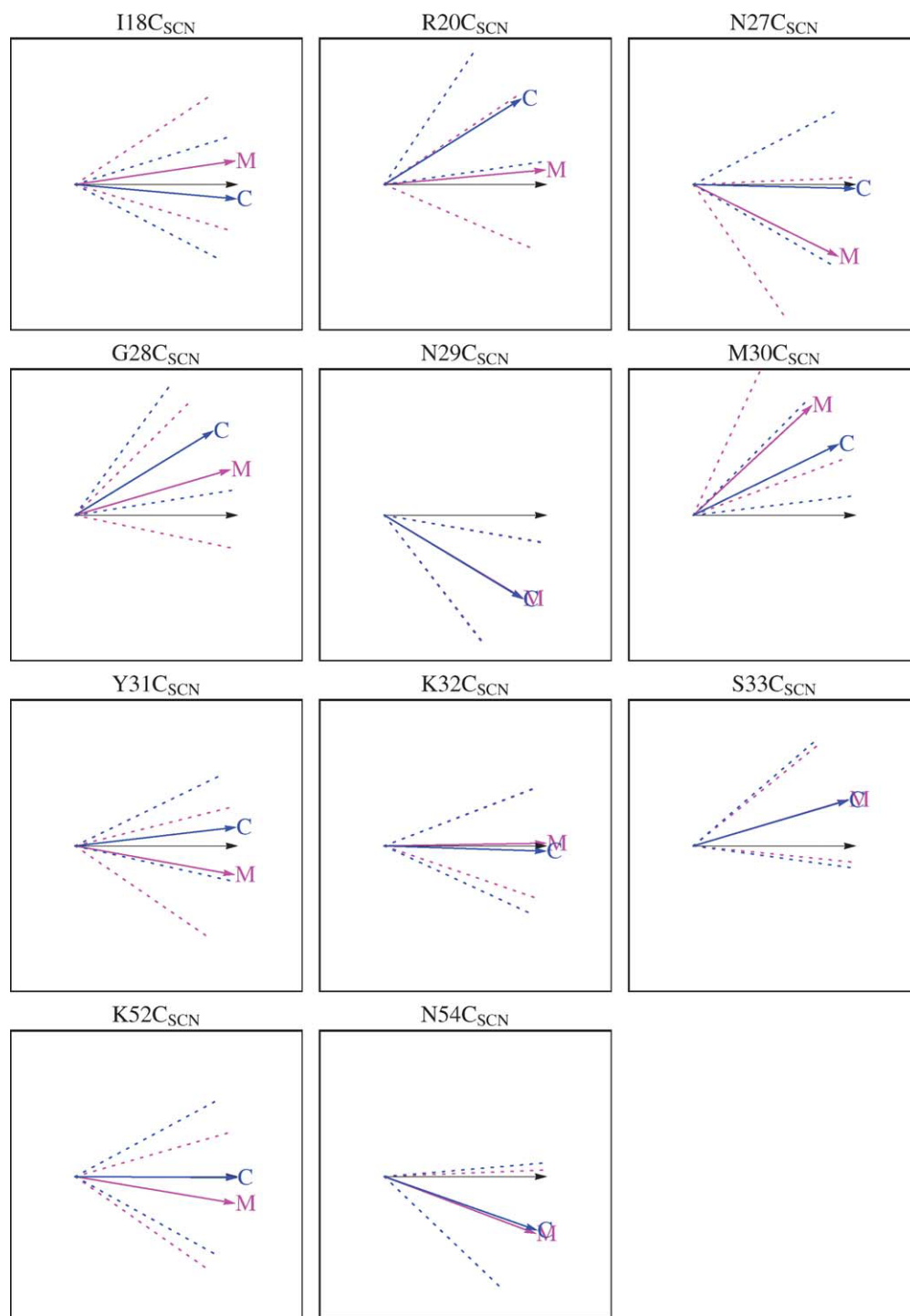
The calculated electrostatic field is correlated neither with the angle or change in angle to the binding surface nor with the angle or change in angle to the polar plane (data not shown). However, there are some interesting features evident in these results. Figure 4 shows the average azimuthal orientation of the nitrile probe relative to the Ras-Ral binding surface. These results show that in 7

**Figure 4**

The average azimuthal orientation of the nitrile probe relative to the Ras-Ral binding surface shown in Figure defined binding surface. “Ras” indicates the Ras side of the interface, which is solvent in the monomeric state (M, magenta) and Ras itself in the docked complex (C, blue). The angle between each pair of dashed lines shows one standard deviation from simulation.

of the 11 mutants the probe swings closer to the Ras surface on binding by a small amount, about 10° . In only one of the other four cases, Ral R20C_{SCN} does the probe

swing toward the Ral mutant’s surface on binding. For the Ral G28C_{SCN}, N29C_{SCN}, and M30C_{SCN}, the probe’s orientation relative to the binding surface does not

**Figure 5**

The average polar orientation of the nitrile probe relative to the binding surface axis in the monomeric (M, magenta) and docked complex (C, blue) states of labeled Ral mutants. The view is looking down onto the Ral binding surface from the Ras side of the binding surface. The angle between each pair of dashed lines show one standard deviation.

appear to change upon binding. In M30C_{SCN}, the probe appears to lie in the plane of the binding surface in both states. In all cases other than this and Ral Y31C_{SCN}, the

probe points, on average, away from the Ral surface in both states; in Y31C_{SCN} it points toward the Ral surface in both cases.

Figure 5 shows the average polar orientation of the nitrile probe relative to a plane perpendicular to the binding surface. These results show that the polar orientation of the probe's projection on the binding surface changes on binding in 7 of the 11 cases; it remains about the same in the N29C_{SCN}, K32C_{SCN}, S33C_{SCN}, and N54C_{SCN} variants of Ral. There are larger swings (greater than half of one standard deviation) in R20C_{SCN}, N27C_{SCN}, M30C_{SCN}, and Y31C_{SCN}. Taken together with the orientations relative to the binding surface, it appears that the only probe that does not change orientation significantly is N29C_{SCN}.

Sources of the electric field

The explicit solvent method to calculate electrostatic fields uses the reaction field electrostatic calculation of GROMACS,⁵² allowing the system to be treated with periodic boundary conditions. To calculate the force at the nitrile, we placed a test charge ($q = +1$) at the nitrile bond midpoint into a molecular dynamics snapshot and calculated the force on that charge using the "rerun" option of the GROMACS molecular dynamics engine, mdrun. The GROMACS reaction field long-range interaction is a modification of Coulomb's law, which considers the energy of interaction between two charges q_1 and q_2 separated by a distance r_{12} to be

$$V = f \frac{q_1 q_2}{\epsilon_r} \left[\frac{1}{r_{12}} + k r_{12}^2 - c \right] \quad (3)$$

where $f = 1 - (4\pi\epsilon_0)$, ϵ_r is the short-range dielectric (here $\epsilon_r = 1$), and

$$k = \frac{1}{r_c^3} \frac{\epsilon_{rf} - \epsilon_r}{2\epsilon_{rf} - \epsilon_r} \quad (4)$$

and

$$c = \frac{1}{r_c} \frac{3\epsilon_{rf}}{2\epsilon_{rf} + \epsilon_r} \quad (5)$$

The scaling distance r_c determines where the potential decays to zero and was chosen to be 1.0 nm for these calculations. The long-range dielectric ϵ_{rf} was chosen to be 78. Like Coulomb's law but in contrast to PB, the reaction field treatment is additive over point charges. For this reason, the explicit solvent field calculation using the reaction field can be used to calculate the electrostatic field from different components of the system. Preliminary computational work underway in our laboratory has suggested that fields calculated in this way correlate strongly with electrostatic fields calculated using Poisson-Boltzmann electrostatics with the same force field, although PB appears to give better results. These results will be reported in detail in a later publication.

The nitrile probe sits in a complicated electrostatic environment formed by contributions from amino acids on both the Ras and Ral surfaces, the solvent, and the GDPNP cofactor and magnesium ion bound to the active site of Ras, which lies about 7 Å from the model binding surface. We used the explicit solvent method with reaction field electrostatics to calculate electrostatic fields at the nitrile midpoint and averaged the results using the Boltzmann distribution of the nitrile orientation derived from WHAM. The contribution to the field from specific components of the system was determined by setting the charges of all other components to zero in the force field. Electrostatic fields at the nitrile were computed for the following components: (1) solvent, including sodium counter ions; (2) amino acid residues on the Ral surface, other than the probe's residue; (3) the probe residue's atoms other than the nitrile; (3) the rest of the Ral molecule; (4) the Ras surface, including the GTP cofactor analog and the magnesium ion; and (5) the rest of the Ras molecule. We considered the Ral surface to include all those residues that were systematically mutated to cysteine in our experiments, that is I18, R20, N27, G28, N29, M30, Y31, K32, S33, K52, and N54. The Ras surface was defined as for the geometric calculations, residues Q25, D33, P34, T35, I36, E37, D38, Y40, R41, and K42. The non-hydrolyzable GTP cofactor analog guanosine GDPNP was present in Ras in our experiments; because this molecule carries of charge of -4 and is associated with the divalent Mg^{2+} ion, this group could significantly impact on the field at some probe locations. For all calculations, the field due to the nitrile carbon and nitrogen atoms was ignored. We compared the field (averaged over the Boltzmann distributions of probe orientation from WHAM) due to different pieces of the system in the monomeric and docked complex states by correlation analysis between monomer and complex fields. Higher values of r^2 and low values of P indicate a stronger linear correlation between fields in the two states.

Field due to solvent

The correlation of electrostatic field due to solvent and solvated sodium ions in the monomer and docked complex is shown in Figure 6. There is a modest correlation ($r^2 = 0.20$, $P = 0.17$) between field due to solvent in each state of Ral. Even though it is weak, this degree of correlation is surprising, because the solvent presumably has greater access to any given probe in the monomeric state, compared with the docked complex where the probes tend to lie (but are not all) between the two proteins. The four mutants that seem to deviate from this pattern most strongly are R20C_{SCN} (mutant 2), M30C_{SCN} (mutant 6), K32C_{SCN} (mutant 8), and S33C_{SCN} (mutant 9). These sites on the Ral surface, together with Y31, are more centrally located on the binding surface, which may

account for the more significant difference in field on binding; in contrast, the field due to solvent at Y31C_{SCN} (which lies close to the edge of the binding surface) appears to be the same in both the monomer and docked complex states. That the field at the other probe sites is nearly equivalent in both states suggests some degree of solvent exposure in the docked state. Experiments exploring the effect of solvent exposure of the SCN probe on the monomeric Ral surface are currently underway in our laboratory, which we believe will provide insight into this finding.

Field due to Ral

Correlations of field contributions from Ral are shown in Figure 7, for both Ral surface residues excluding cyanocysteine [Fig. 7(a)], the nonsurface residues of Ral [Fig. 7(b)], and the cyanocysteine [Fig. 7(c)]. For the correlation of Ral surface fields between the monomeric and docked complex states, the correlation is more significant than solvent ($r^2 = 0.31$, $P = 0.075$); the field due to the Ral surface is similar in the monomeric and docked complex states. The correlation is stronger for the nonsurface residues of Ral ($r^2 = 0.72$, $P = 0.001$). The field due to the cyanocysteine side chain has a correlation between the monomeric and docked complex states of $r^2 = 0.60$, $P = 0.053$. These high correlations indicate that, on average, docking with Ras does not strongly perturb the field due to Ral at the probe. Of these three, the most significant changes are in the Ral surface residues, which experience substantially different environments in the bound and unbound states. Nevertheless, the Ral surface fields are similar in both states, consistent with the observation of subtle probe reorientations described in the previous section. We have begun experiments to test the effect of mutations at the Ral surface on the magnitude and direction of electrostatic fields experienced by SCN probes at the Ral surface.

Field due to Ras

The contributions of Ras to the change in electric field are compared with the contributions of Ral and solvent in Figure 8. The total change in field on binding is composed of (1) the change in field due to the perturbation of the solvent charge distribution, (2) the change in field due to perturbation of the Ral charge distribution, and (3) introduction of the Ras charge distribution. Contributions (1) and (3) are intimately related, as solvent at the Ral surface is displaced upon binding of Ras. For six of the 11 mutants (I18C_{SCN}, R20C_{SCN}, N27C_{SCN}, K32C_{SCN}, and K52C_{SCN}), the largest contribution is from the addition of Ras; these probes are potentially the best located to inform on Ras fields. However, for four others (N29C_{SCN}, Y31C_{SCN}, S33C_{SCN}, and N54C_{SCN}), the largest contribution is from Ral, indicating that these probes may be better suited to the investigation of changes that

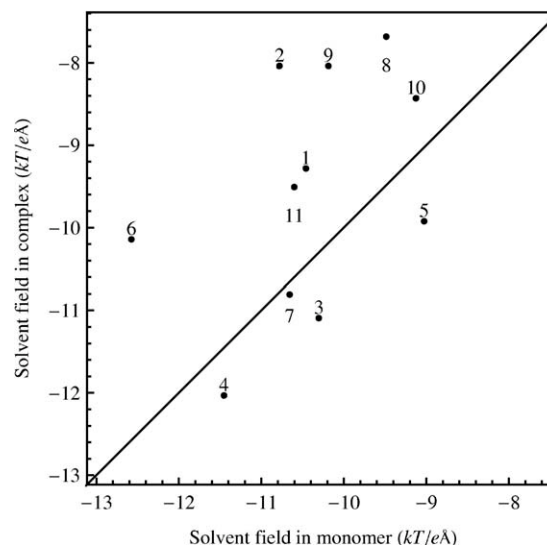


Figure 6

Comparison of electrostatic fields due to solvent in the monomeric (horizontal axis) and docked complex (vertical axis) states of Ral. Numbers refer to mutants of Ral surface residues shown in Figure 2. The line shown is $y = x$, not a linear fit. There is a weak correlation between solvent fields in the two states, $r^2 = 0.20$, $P = 0.17$. However, the field due to solvent is similar in most cases between the bound and unbound states, and so on average the solvent field cancels in the Stark effect calculation. The outliers R20C_{SCN} (mutant 2), M30C_{SCN} (mutant 6), K32C_{SCN} (mutant 8), and S33C_{SCN} (mutant 9) are located in the middle of the binding surface and are expected to be more secluded from solvent in the docked complex state.

occur to the Ral surface on binding. The final mutant, M30C_{SCN}, has its the largest contribution to the total electric field from solvent, but contributions changes in field due to Ras and Ral conspire to cancel the field change due to solvent.

DISCUSSION

Our vibrational Stark effect experiments⁹ are intended to map electrostatic fields on the Ras surface and to understand its role in the docking interaction. Significant contribution to ΔF from structural rearrangement of Ral on binding could potentially introduce significant noise, rendering such interpretations unfeasible. These contributions could originate from global changes in the Ral molecule, or from reorientation of the nitrile probe on a fixed Ral surface. However, Figures 4 and 5 show minor changes in probe orientation on binding, in most cases. This is confirmed by the high degree of correlation between fields due to the non-nitrile atoms of the cyanocysteine side chain in the model ($r^2 = 0.60$, $P = 0.053$); one might expect significant changes in the field to originate from the nearest charges (i.e., the atoms on the cyanocysteine residue itself) if large reorientations occurred on binding, but this appears not to be the case.

Furthermore, the correlation of Ral nonsurface fields ($r^2 = 0.72$, $P = 0.001$) indicates statistically identical contributions to the field and therefore very little global rearrangements of the Ral molecule, other than the surface, in the docked complex state. The largest contributions to ΔF from Ral tend to be from the Ral surface, which is

weakly correlated between the two states ($r^2 = 0.31$, $P = 0.075$). On average, the contribution to ΔF from changes in Ral tend to be smaller than contributions from Ras, suggesting that our experiments are, as intended, capable of mapping the electrostatic fields of the Ras surface without overwhelming noise from Ral structural rearrangements. However, if rearrangements of Ral contribute significantly to electric field shifts, these results suggest that they are most commonly due to rearrangements of nearby residues on the Ral surface. We are currently testing this hypothesis experimentally, which will be discussed in a future report.

The probes that have the largest relative contributions to ΔF from changes in Ral are R20C_{SCN} (mutant 2), N29C_{SCN} (mutant 5), Y31C_{SCN} (mutant 7), S33C_{SCN} (mutant 9), and N54C_{SCN} (mutant 11). These calculations therefore indicate that Ral structural rearrangements contribute a significant amount to the field shifts observed in experiment. Of these, Ral is the single largest relative contributor to ΔF for N29C_{SCN}, Y31C_{SCN}, and N54C_{SCN} (Fig. 8). The contribution from Ral to field shifts for R20C_{SCN}, N29C_{SCN}, and Y31C_{SCN} is almost wholly due to the Ral surface. In contrast, N54C_{SCN} is the most significant outlier in Figure 7(c); the largest contribution to its ΔF of 2.8 kT/eÅ is from Ral, and this is predominantly from nonsurface residues. The comparative insensitivity of other residues to Ral amino acids that are not at the Ral surface suggests that the loop containing this probe actually shifts on binding, relative to the Ral molecule, or the motion of nearby nonsurface residues. N54C_{SCN} is the most C-terminal of our probes, and in these calculations may be sensitive to fluctuations in the 4 modeled C-terminal residues. S33C_{SCN} has a significant change in field due to solvent, opposite in sign and of similar magnitude than the contribution from Ral; the total ΔF for this mutant is smaller in magnitude than either solvent or Ral fields. This is also a poor probe of the Ras surface. If the predictions of insensitivity to the Ras surface are correct for these five probes, they may still be useful probes of vibrational Stark effect experiments aimed at examining fields in other parts of

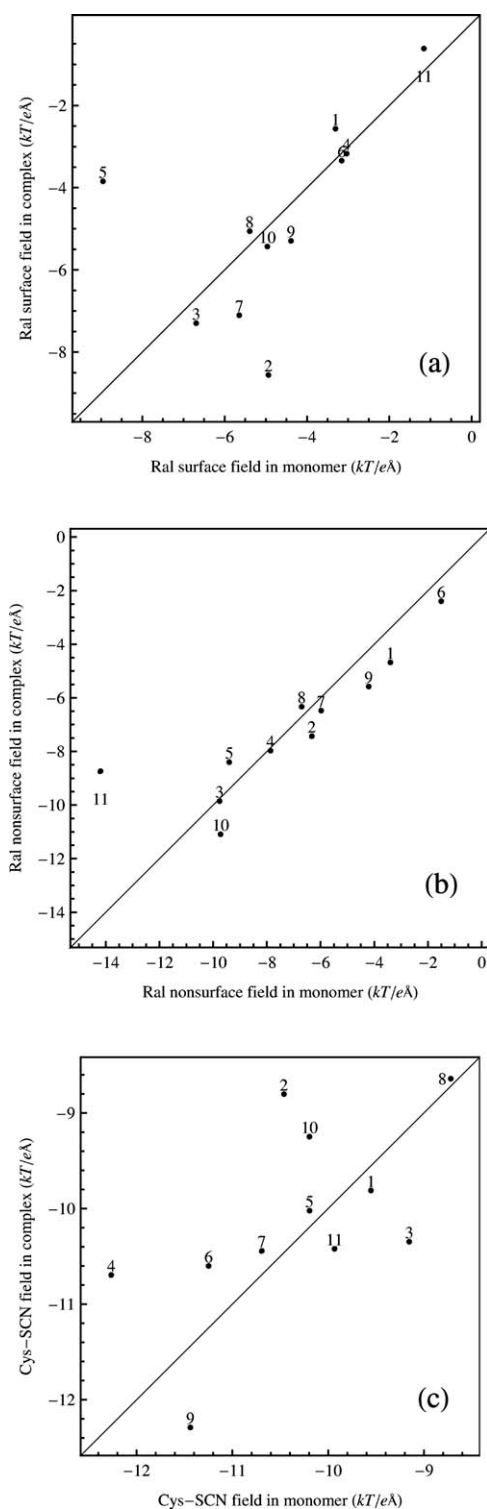
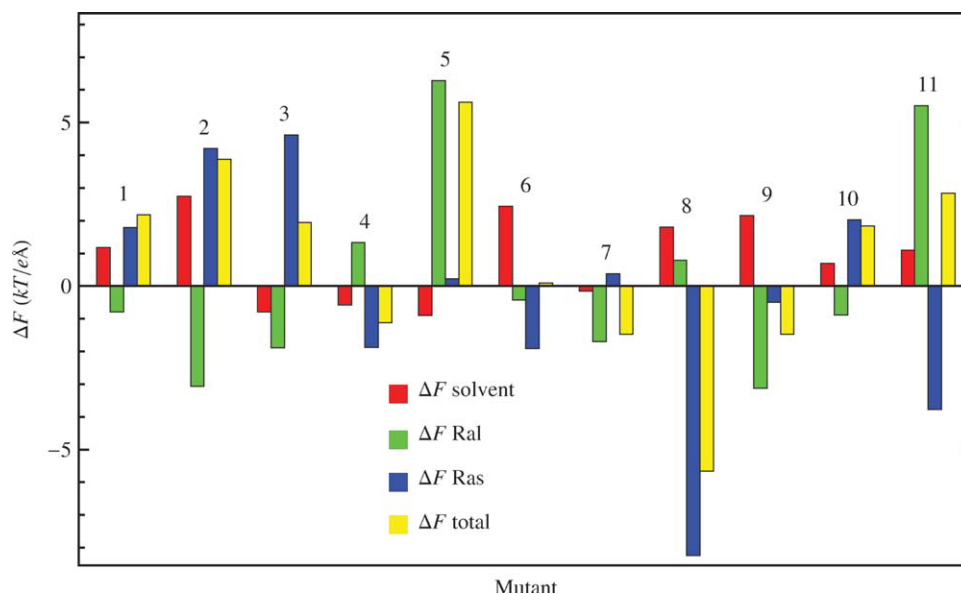


Figure 7

Comparison of electrostatic fields due to Ral; for each plot, the field due to a selected subset of Ral residues is shown on the horizontal axis for the monomeric state and the vertical axis for the docked complex. (a) Comparison of electrostatic fields due to the 11 Ral surface residues, excluding cyanocysteine atoms. (b) Comparison of electrostatic fields due to Ral residues other than the 11 surface residues. (c) Comparison of electrostatic fields due to cyanocysteine atoms, excluding the nitrile group itself. Numbers refer to mutants of Ral surface residues shown in Figure 2. The lines shown are $y = x$, not linear fits. The correlations between Ral fields in each state have $r^2 = 0.31$, $P = 0.075$ for the Ral surface residues and $r^2 = 0.72$, $P = 0.001$ for nonsurface residues. The correlations between cyanocysteine fields are $r^2 = 0.60$, $P = 0.053$. On average, the electrostatic field at the nitrile due to Ral is the same in both states and effectively the Ral field cancels in the Stark effect calculation.

**Figure 8**

Contributions to the total change in electric field. Numbers refer to mutants of Ral surface residues shown in Figure 2. The total change in field contributions include the change in solvent field upon binding (ΔF solvent), change in Ral field on binding (ΔF Ral), and the change in field due to the addition of Ras (ΔF Ras). These three contributions add up to the total field, ΔF total.

the system: the solvent for mutant 9, and the Ral surface itself for mutants 5 and 7, and the C-terminus for the probe at position 54, N54C_{SCN}.

The computational results for most of the other probes are consistent with the hypothesis that observed Stark shifts are caused by binding of Ral to Ras and not by structural relaxation. The most reliable probes of the docking interaction are those with the smallest relative contributions to ΔF from Ral, I18C_{SCN} (mutant 1), R20C_{SCN} (mutant 2), N27C_{SCN} (mutant 3), G28C_{SCN} (mutant 4), K32C_{SCN} (mutant 8), and K52C_{SCN} (mutant 10). We have already discussed R20C_{SCN} above; this probe has significant contributions to the total field from all three components of the system (Ras, Ral, and solvent) and for this reason may be the poorest overall probe. When the probe is at positions I18C_{SCN} and R20C_{SCN}, they both experience contributions from solvent, which are almost as large as the contributions from Ras; it is possible that Stark effects for these probes directly not only reflect the Ras electrostatic field but also the removal and/or rearrangement of nearby water molecules. This is a natural part of the docking interaction, and although these three mutants do not directly probe the Ras surface they strongly reflect the docking interaction both through changes in solvent and the introduction of Ras. Probes N27C_{SCN}, G28C_{SCN}, K32C_{SCN}, and K52C_{SCN}, in contrast, are the best located to probe the Ras electrostatic field, as shown in Figure 8. The most important contribution to ΔF for these probes is the introduction of Ras itself.

The last probe, M30C_{SCN} (mutant 6) is unique among the 11 probes in these calculations. Unlike any other

probe, at this position, the thiocyanate experiences a very small change in field, 0.1 kT/eÅ. The largest contributions, solvent (2.4 kT/eÅ) and Ras (−1.9 kT/eÅ), are of similar magnitude and opposite sign and much larger than the total change. There is little contribution from Ral (−0.4 kT/eÅ), consistent with minimal probe rearrangements in Figures 4 and 5. This mutant may be uniquely sensitive to changes in solvent in the monomeric state (e.g., changes in pH or ionic strength) or mutations to Ras in the docked complex, but not to docking or mutations to Ral. Testing this will be the subject of future experiments.

CONCLUSIONS

In this report, we demonstrate that investigation of electrostatic fields by means of explicit solvent calculations allows physical insight into the origin of these fields in this system that would be difficult to determine experimentally, because experiments cannot ignore the charges of certain parts of the system. These calculations, together with the information regarding probe orientation in both the monomeric and docked states, provide powerful insight into experimentally measured electrostatic fields⁹ and suggest new experimental directions. In particular, the strong correlation of Ral fields between the monomer and docked complex states (Fig. 7) indicates that Ral largely carries its field from state to state. This has interesting implications for Ras-effector interactions and is currently being tested experimentally in our laboratory. Further, our geometrical obser-

vations demonstrate that the probe undergoes no significant structural perturbation on binding. This is consistent with the observation that labeling with the nitrile VSE spectroscopic probe does not alter the rate of formation of the docked complex, measured by the dissociation constant of the Ras-Ral complex.⁹ Changes in absorption energy of the nitrile on complex formation are, therefore, a reasonable and valid measurement of electrostatic fields created by the binding of Ras, rather than structural rearrangement of the Ral surface. Taken together, our results confirm that VSE spectroscopic experiments are measuring the different electrostatic environments presented by solvent in the Ral monomer, and the Ras surface in the Ras-effector docked complex. This study demonstrates the utility of combining VSE experimental and computational investigations to explore the physical origin and effects of electrostatic fields at the protein-protein interface.

ACKNOWLEDGMENTS

LJW Holds a Career Award at the Scientific Interface from the Burroughs Wellcome Fund. The authors acknowledge the Texas Advanced Computing Center (TACC) at The University of Texas at Austin for providing high-performance computing resources that have to contributed to the results reported within this paper.

REFERENCES

- Shields J, Pruitt K, McFall A, Shaub A, Der C. Understanding Ras: 'it ain't over 'til it's over. *Trends Cell Bio* 2000;10:147–154.
- Cox A, Der C. The dark side of Ras: regulation of apoptosis. *Oncogene* 2003;22:8999–9006.
- Downward J. Targeting ras signalling pathways in cancer therapy. *Nature Rev Cancer* 2003;3:11–22.
- Repasky G, Chenette E, Der C. Renewing the conspiracy theory debate: does Raf function alone to mediate Ras oncogenesis? *Trends Cell Bio* 2004;14:639–647.
- Harvey J. An Unidentified Virus which causes the Rapid Production of Tumours in Mice. *Nature* 1964;204:1104–1105.
- Bos J. Ras oncogenes in human cancer: A review. *Cancer Res* 1989;49:4682–4689.
- Sprang S. G protein mechanisms: Insights from structural analysis. *Annu Rev Biochem* 1997;66:639–678.
- Krauss G. *Biochemistry of signal transduction and regulation*, 3rd ed.; Weinheim, Germany: Wiley VCH Verlag; 2003.
- Stafford AJ, Ensign DL, Webb LJ. Vibrational stark effect spectroscopy at the interface of Ras and Rap1A bound to the Ras binding domain of RalGDS reveals an electrostatic mechanism for protein-protein interaction. *J Phys Chem B* 2010;114:15331–15344.
- Andrews S, Boxer S. Vibrational stark effects of nitriles I. Methods and experimental results. *J Phys Chem A* 2000;104:11853–11863.
- Andrews S, Boxer S. Vibrational stark effects of nitriles II. Physical origins of stark effects from experiment and perturbation models. *J Phys Chem A* 2002;106:469–477.
- Suydam I, Boxer S. Vibrational stark effects calibrate the sensitivity of vibrational probes for electric fields in proteins. *Biochemistry* 2003;42:12050–12055.
- Fafarman AT, Webb LJ, Chuang JI, Boxer SG. Site-specific conversion of cysteine thiols into thiocyanate creates an IR probe for electric fields in proteins. *J Am Chem Soc* 2006;128:13356–13357.
- Suydam IT, Snow CD, Pande VS, Boxer SG. Electric fields at the active site of an enzyme: direct comparison of experiment with theory. *Science* 2006;313:200–204.
- Webb LJ, Boxer SG. Electrostatic fields near the active site of human aldose reductase: 1. New inhibitors and vibrational stark effect measurements. *Biochemistry* 2008;47:1588–1598.
- Fafarman AT, Boxer SG. Nitrile bonds as infrared probes of electrostatics in ribonuclease S. *J Phys Chem B* 2010;114:13536–13544.
- Warshel A, Levitt M. Theoretical studies of enzymic reactions: Dielectric, electrostatic, and steric stabilization of carbonium-ion in reaction of lysozyme. *J Mol Biol* 1976;103:227–249.
- Davis M, McCammon J. Electrostatics in biomolecular structure and dynamics. *Chem Rev* 1990;90:509–521.
- Honig B, Nicholls A. Classical electrostatics in biology and chemistry. *Science* 1995;268:1144–1149.
- Baker N, Sept D, Joseph S, Holst M, McCammon J. Electrostatics of nanosystems: application to microtubules and the ribosome. *PNAS* 2001;98:10037–10041.
- Karp D, Stahley M, Garcia-Moreno E. *Biochemistry* 2010.
- van Gunsteren W, Billeter S, Eising A, Hünenberger P, Krüger P, Mark P, Tironi I. *Biomolecular simulation: The GROMOS96 manual and user guide*. Zürich, Switzerland: Hochschulverlag AG an der ETH Zürich; 1996.
- MacKerell AD, Jr. Computational biochemistry and biophysics. In: Becker OM, Mackerell AD, Jr, Roux B, Watanabe M, editors. *Atomistic models and force fields*. New York: Marcel Dekker, Inc., 2001; pp 7–38.
- Duan Y, Wu C, Chowdhury S, Lee M, Xiong G, Zhang W, Yang R, Cieplak P, Luo R, Lee T, Caldwell J, Wang J, Kollman P. A point-charge force field for molecular mechanics simulations of proteins based on condensed-phase quantum mechanical calculations. *J Comput Chem* 2003;24:1999–2012.
- Warshel A, Kato M, Pislakov A. *J Chem Theory Comput* 2007;3:2034–2045.
- Ponder JW, Wu C, Ren P, Pande VS, Chodera JD, Schnieders MJ, Haque I, Mobley DL, Lambrecht DS, DiStasio RA, Jr, Head-Gordon M, Clark GNI, Johnson ME, Head-Gordon T. Current status of the AMOEBA polarizable force field. *J Phys Chem B* 2010;114:2549–2564.
- Pearson J, Oldfield E, Lee F, Warshel A. Chemical-shifts in proteins: A shielding trajectory analysis of the fluorine nuclear-magnetic-resonance spectrum of the Escherichia-coli galactose binding-protein using a multipole shielding polarizability local reaction field molecular-dynamics approach. *J Am Chem Soc* 1993;115:6851–6862.
- Danielson M, Falke J. Use of F-19 NMR to probe protein structure and conformational changes. *Ann Rev Biophys Biomol Struct* 1996;25:163–195.
- Schutz C, Warshel A. What are the dielectric “constants” of proteins and how to validate electrostatic models? *Proteins Struct Funct Genet* 2001;44:400–417.
- Forsyth W, Antosiewicz J, Robertson A. Empirical relationships between protein structure and carboxyl pK(a) values in proteins. *Proteins Struct Funct Genet* 2002;48:388–403.
- Thurkill RL, Grimsley GR, Scholtz M, Pace CN. Hydrogen bonding markedly reduces the pK of buried carboxyl groups in proteins. *J Mol Biol* 2006;362:594–604.
- Matousek WM, Ciani B, Fitch CA, Garcia-Moreno EB, Kammerer RA, Alexandrescu AT. Electrostatic contributions to the stability of the GCN4 leucine zipper structure. *J Mol Biol* 2007;374:206–219.
- Baran K, Chimenti M, Schlessman J, Fitch C, Herbst K, Garcia-Moreno B. Electrostatic effects in a network of polar and ionizable groups in staphylococcal nuclease. *J Mol Biol* 2008;379:1045–1062.
- Castaneda C, Fitch C, Majumdar A, Khangulov V, Schlessman J, Garcia-Moreno B. Molecular determinants of the pK(a) values of Asp and Glu residues in staphylococcal nuclease. *Proteins Struct Funct Bioinformatics* 2009;77:570–588.

35. Harms MJ, Castaneda CA, Schlessman JL, Sue GR, Isom DG, Cannon BR, Garcia-Moreno EB. The pK(a) values of acidic and basic residues buried at the same internal location in a protein are governed by different factors. *J Mol Biol* 2009;389:34–47.
36. Case DA, Darden TA, Cheatham TE, Simmerling CL, Wang J, Duke RE, Luo R, Walker RC, Zhang W, Merz KM, Roberts BP, Wang B, Hayik S, Roitberg AE, Seabra G, Kolossvy I, Wong KF, Paesani F, Vanicek J, Wu X, Brozell SR, Steinbrecher T, Gohlke H, Cai Q, Ye X, Wang J, Hsieh MJ, Cui G, Roe DR, Mathews DH, Seetin MG, Sagui C, Babin V, Luchko T, Gusarov S, Kovalenko A, Kollman PA. 2010, AMBER 11, University of California, San Francisco.
37. Cieplak P, Cornell W, Bayly C, Kollman P. Application of the multi-molecule and multiconformational RESP methodology to biopolymers: charge derivation for DNA, RNA, and proteins. *J Comp Chem* 1995;16:1357–1377.
38. Schmidt M, Baldrige K, Boatz J, Elbert S, Gordon M, Jensen J, Koseki S, Matsunaga N, Nguyen K, Su S, Windus T, Dupuis M, Montgomery J. General atomic and molecular electronic-structure system. *J Comp Chem* 1993;14:1347–1363.
39. Gordon MS, Schmidt MW. Theory and applications of computational chemistry: the first forty years. Amsterdam: Elsevier, 2005. pp 1167–1189.
40. Van der Spoel D, Lindahl E, Hess B, Groenhof G, Mark A, Berendsen H. GROMACS: Fast, flexible, and free. *J Comp Chem* 2005;26:1701–1718.
41. Sorin E, Pande V. Exploring the helix-coil transition via all-atom equilibrium ensemble simulations. *Biophys J* 2005;88:2472–2493.
42. Wang J, Wolf R, Caldwell J, Kollman P, Case D. Development and testing of a general amber force field. *J Comput Chem* 2004;25:1157–1174.
43. Wang J, Wang W, Kollman PA, Case DA. Automatic atom type and bond type perception in molecular mechanical calculations. *J Mol Graph Model* 2006;25:247–260.
44. Pulay P. Convergence acceleration of iterative sequences: the case of SCF iteration. *Chem Phys Lett* 1980;73:393–398.
45. Cornell W, Cieplak P, Bayly C, Gould I, Merz K, Ferguson D, Spellmeyer D, Fox T, Caldwell J, Kollman P. A 2nd generation force field for the simulation of proteins, nucleic acids and organic molecules. *J Am Chem Soc* 1995;117:5179–5197.
46. Avogadro: an open-source molecular builder and visualization tool. Version 1.00. <http://avogadro.openmolecules.net/>.
47. Jorgensen W, Chandrasekhar J, Madura J, Impey R, Klein M. Comparison of simple potential functions for simulating liquid water. *J Chem Phys* 1983;79:926–935.
48. Roux B. The calculation of the potential of mean force using computer simulations. *Comput Phys Commun* 1995;91:275–282.
49. Gallicchio E, Andrec M, Felts A, Levy R. Temperature weighted histogram analysis method, replica exchange, and transition paths. *J Phys Chem B* 2005;109:6722–6731.
50. Humphrey W, Dalke A, Schulten K. “VMD - Visual Molecular Dynamics”. *J Molec Graphics* 1996;14:33–38.
51. Russell R, Barton G. Proteins: *Struct Funct Genet* 1992;14:309–323.
52. van der Spoel, D, Lindahl E, Hess B, van Buuren, AR, Hess B, van Buuren A, Apol E, Meulenhoff P, Tieleman D, Sijbers A, Feenstra K, van Drunen R, Berendsen H. Gromacs User Manual version 4.0. Available at: www.gromacs.org, 2005.